Available online at www.sciencedirect.com
SCIENCE DIRECT®
Earth and Planetary Science Letters 243 (2006) 632–649
EPSL
www.elsevier.com/locate/epsl

Seismic characterization of mantle flow in subduction systems: Can we resolve a hydrated mantle wedge?

Teresa Mae Lassak [a,*], Matthew J. Fouch [a], Chad E. Hall [b], Édouard Kaminski [c]

[a] Department of Geological Sciences, Arizona State University, Tempe, AZ 85287-1404, United States
[b] Seismological Laboratory, California Institute of Technology, Pasadena, CA 91125, United States
[c] Laboratoire de Dynamique des Systèmes Géologiques, IPG Paris and Université Paris 7, FR 75252, France

Received 19 August 2005; received in revised form 10 January 2006; accepted 11 January 2006
Available online 2 March 2006
Editor: S. King

Abstract

This study provides new constraints on the resolvability of mantle flow in subduction zone settings as inferred by observations of seismic anisotropy. We are motivated by the broad range of shear wave splitting observations in subduction systems that suggest complex flow geometries, changes in the deformation state of mantle minerals, or a combination of both. While shear wave splitting fast polarization directions are typically interpreted as a proxy for flow or maximum finite extension, experimental studies suggest that olivine slip systems change under higher stress and hydration states, conditions likely appropriate for subduction systems. In this study, we predict shear wave splitting as a result of mantle silicate lattice-preferred orientation development in steady-state two-dimensional mantle flow models using a textural development theory that incorporates the combined effects of intracrystalline slip and dynamic recrystallization. We utilize the resulting textures to predict shear wave splitting for populations of seismic raypaths traversing the model within the subduction zone mantle wedge. The results of our study demonstrate that combined observations of variations in fast polarization directions and splitting times make it possible to resolve a shift from anhydrous to hydrous mantle insubduction zone settings provided very good sampling of the mantle wedge. Our models are generally consistent with observed splitting variations for several subduction zones with dense data sampling, including Tonga, Japan, and Kamchatka. The implications of our work suggest that, provided adequate data sampling, shear wave splitting measurements can provide the necessary information to evaluate potential competing effects between variations in mantle flow direction and changes in the stress and hydration states of subduction zone mantle wedges.
© 2006 Elsevier B.V. All rights reserved.

Keywords: subduction zones; shear wave splitting; lattice-preferred orientation; mantle flow

1. Introduction

As part of the convective system that mobilizes Earth's mantle, subduction zones are one of the key expressions of plate tectonics. Convergent margins represent an important setting to study the processes of arc volcanism, seismicity, and deformation, which are influenced by thermal, rheological, and compositional factors. In particular, understanding the relationship between deformation and resulting fabric in the mantle wedge between subducting and overriding lithospheric

* Corresponding author. Tel.: +1 480 965 5081; fax: +1 480 965 8102.
E-mail address: Teresa.Lassak@asu.edu (T.M. Lassak).

0012-821X/$ - see front matter © 2006 Elsevier B.V. All rights reserved.
doi:10.1016/j.epsl.2006.01.022

plates is essential to improving our understanding of the subduction factory. Significant progress in constraining mantle wedge processes has been made from seismological observations, mineral physics experiments, and geodynamic models [1–5], but linking results from these fields remains a significant challenge. Of particular importance is providing an improved understanding of the influence of mantle hydration and its effects on inferring mantle wedge deformation using seismic observations [6,7].

Subduction zones exhibit a broad range of mantle seismic anisotropy observations which are inferred to express dominant deformational processes in this tectonic setting. A particularly well-studied manifestation of seismic anisotropy is shear wave splitting (SWS). Observations of SWS are comprised of a fast polarization direction, which reflects the orientation of fabric, and a splitting time, which reflects the organization and strength of the fabric. In many cases, a range of fast polarization directions has been documented within the same subduction system, such as in Tonga (e.g., [8–10]), Japan (e.g., [11,12]), Kamchatka (e.g., [13,14]), and South America (e.g., [15–17]) (Fig. 1). These sometimes discrepant observations hint at the complex array of dynamic processes that occur near subduction zones.

Seismic anisotropy in the mantle is generally assumed to be the result of lattice-preferred orientation (LPO) of mantle minerals such as olivine. For systems with little or no hydration, LPO of olivine *a*-axes (the seismically fastest axis for shear waves) are assumed to be aligned with the direction of flow in the dislocation creep regime (e.g., [18,19]). Conversely, experimental studies suggest that olivine slip systems change under higher stresses and hydration states [4]. Since some subduction zones are likely regions of high stress and hydration (e.g., [20]), the development of olivine LPO in these regions may be significantly different [4,21,22].

An extensive range of models for subduction zone flow and deformation have been developed (e.g., [23–26]). While important advances have been made to connect deformation in flow models with seismic anisotropy observations (e.g., [9,27]), more detailed links between geodynamical models and observed seismic anisotropy for subduction zones can yield significantly improved insight into SWS observations. Additionally, understanding the role mantle hydration plays in seismic anisotropy development due to deformation can improve interpretations of shear wave splitting parameters. Here we provide important new connections between subduction zone flow models and

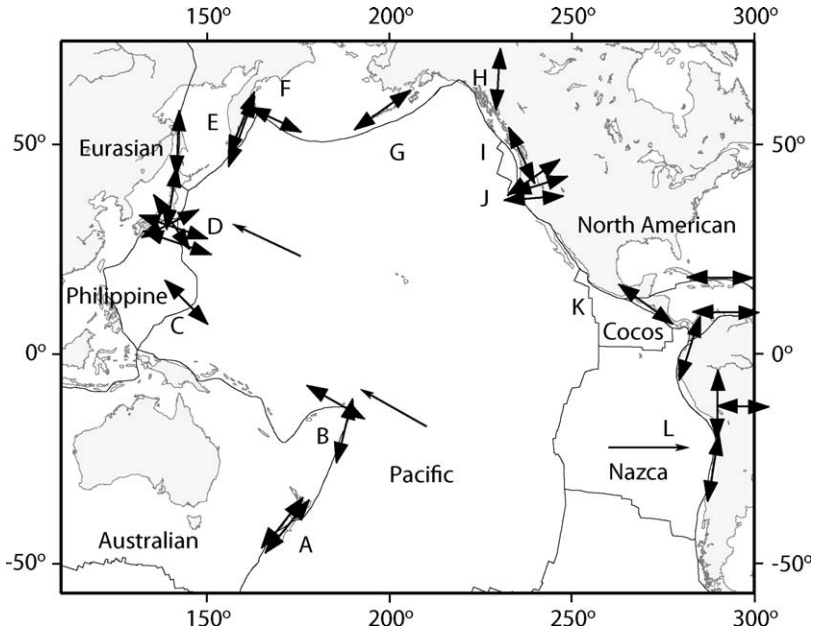

Fig. 1. Summary of shear wave splitting observations around the Pacific Rim illustrating the variety of observed fast directions near subduction zones. Double-headed vectors indicate the average regional orientation of the fast polarization direction. Many regions exhibit fast direction populations with orientations both parallel and orthogonal to local trench strike, including New Zealand (A) [41,57–59], Tonga–Kermadec (B) [8,10,42], Philippines (C) [37,60], Japan (D) [11,12,33,43–47], Kamchatka (E and F) [13,14], Aleutian Islands (G) [61], Alaska (H) [62], Cascadia and Western US (I and J) [63–67], Caribbean (K) [54,68], and South America (L) [15–17].

the seismic manifestation of flow for a range of hydration states in the mantle.

In this study, we examine the connections between dynamic flow models and seismic anisotropy to interpret deformation in subduction systems. We assume that the bulk of observed seismic anisotropy in subduction zones likely results from fabric in the mantle wedge and focus on wedge deformation as imaged by seismic anisotropy observations. To provide intuition regarding how a shift from anhydrous to hydrous olivine is manifested in shear wave splitting observations, we examine simple shear models with a first order transition in olivine hydration state. We then apply this approach to determine the patterns of shear wave splitting measurements that would develop from a hydrated wedge by examining a range of models with anhydrous and hydrated mantle wedge regions. Finally, we relate our results to subduction zones around the Pacific Rim to evaluate SWS observations in these regions.

2. Causes of seismic anisotropy in subduction systems

There are several possible causes of seismic anisotropy. Shape-preferred orientation (SPO) can result from cracks in the crust, melt-filled cracks, or lenses in the mantle (e.g., [2]). SPO may exist in areas beneath mid-ocean ridges and subduction zones in the uppermost mantle, as well as in the lowermost mantle (e.g., [28]) LPO results from mineral alignment during strain (e.g., [4,6,19]), and is inferred to be the dominant cause of upper mantle anisotropy (e.g., [2,8,29–32]). Mantle flow (e.g., [2,22]) and crustal shearing (e.g., [33]) are examples of LPO-producing deformation. Subduction zones are regions where both LPO and SPO may influence seismic anisotropy. In this study, we assume that LPO is the dominant cause of observed anisotropy in the mantle wedge.

Constraining links between mantle deformation and olivine LPO is a field of active study. In a simple anhydrous olivine system, LPO development in unhydrated olivine typically parallels the direction of maximum finite extension or shear (e.g., [18,19,24]). Conversely, hydrous olivine systems possess more complicated LPO effects due to a change in the olivine slip system [4]. Deformation experiments on olivine aggregates deformed under high stress (>340 MPa) and high water content (>200 ppm) at a temperature of 1470 K [4] develop a "type-B" fabric in which *a*-axes align orthogonally to the shear direction but parallel to the shear plane due to a change in dominant slip system. In subduction systems, the presence of water, therefore, potentially influences the orientation and strength of mantle fabric and thus may complicate the interpretation of seismic anisotropy [4,34]. The primary goal of this study is to examine how this complication may directly affect SWS measurements.

3. Predicting shear wave splitting from mantle flow models

In this section, we present the methodology for linking models of mantle flow with predictions of SWS patterns for subduction zone settings following the general approach of Fischer et al. [9], Kaminski and Ribe [5], Fouch et al. [35], and Hall et al. [27]. In its original form, this methodology consists of utilizing the velocity field from mantle flow models to predict LPO development and resulting SWS. These previous studies mapped LPO for mantle mineralogies by either a) orienting crystallographic axes to the local flow direction or b) calculating finite strain directions and using them as a guide for the orientation of crystallographic axes (e.g., [5,6,9,21,27,35]). Of particular significance in this study is the incorporation of a more appropriate LPO calculation methodology developed by Kaminski and Ribe coworkers [5]. This approach incorporates the effects of both plastic deformation and dynamic recrystallization during LPO development in an aggregate of individual crystals. The advantage of this approach over similar methods is that it enables the incorporation of a broader range of mantle mineralogies, including those fabrics developed in high-stress and high-water content olivine deformation experiments described by Jung and Karato [4].

3.1. Calculation of lattice-preferred orientation from flow models

A broad range of approaches for estimating LPO has been developed. One simple approach is to assume finite deformation as a proxy for flow and LPO [24,27], mapping LPO to the direction of flow by assuming that olivine *a*-axes are parallel to flow (e.g., [7,27,35]). A more comprehensive approach is the viscoplastic self-consistent (VPSC) method [3,36] which tracks the evolution of the yield strength of an olivine aggregate, slip system activity and LPO development while accounting for dislocation glide, but not for the effects of dynamic recrystallization. Since dynamic recrystallization has been shown to be an important process in LPO development we therefore utilized the approach introduced by Kaminski and Ribe [5,21] which tracks

the LPO evolution in a flow field by accounting for the effects of both intercrystalline slip and dynamic recrystallization (DRex) [21]. The advantages of the DRex approach are that it can incorporate a range of flow models and various mineralogies (i.e., olivine, enstatite, or an olivine/enstatite mixture) and that it is computationally efficient.

DRex estimates the deformation of individual crystals in an aggregate as a function of orientation and slip system activity. The dislocation density of the grains is calculated from their deformation as a function of two parameters, grain-boundary mobility and nucleation coefficient, which have been constrained by experimental results for LPO development in simple shear [4–6]. In this formulation, the evolution of LPO in an aggregate results from the balance between plastic deformation of the grains, which increases dislocation density and thus strain energy, and dynamic recrystallization, which reduces strain energy by consuming dislocations via nucleation and grain boundary migration. The evolution of LPO continues since the orientations of individual crystals in the aggregate favor the maximum strain rate on their softest slip system.

Increased levels of LPO development eventually wane as local strain energy homogenizes within the aggregate. Using the velocities and velocity gradients derived from flow calculations, we model LPO development by tracking natural strain for particles within the flow field. Strain for each particle is tracked along a streamline from its initial position to the location where a maximum natural strain of 5 is reached, which was selected to prevent overwriting of strain history for each aggregate. For the flow fields used in our study, we documented LPO development using values for significant dimensionless parameters based on a series of theoretical tests from Kaminski [6] and Kaminski et al. [21]: grain boundary mobility (M^*), grain nucleation parameter (λ^*), threshold volume fraction (X^*), and the reference critically resolved shear stress for each slip system. M^* characterizes the efficiency of grain boundary migration and is set to a value of 125. Kaminski et al. [21] illustrated the effects of M^* on the LPO in an olivine aggregate, where larger values of M^* lead to more rapid LPO development at lower strains corresponding to warmer environments, while smaller values of M^* lead to retarded LPO development at lower strains corresponding to a cooler environment. We chose $M^* = 125$ for our analyses, but also discuss the effects of varying M^* values in Section 4.1. λ^* characterizes the efficiency of nucleation and is set to a value of 5 in our LPO calculations based on tests by Kaminski et al. [21]. X^* is the ratio of the initial grain size to the grain size allowed for grain boundary sliding. We tested a range of X^* values and chose a value 0.3 as it is within the experimental range determined by Kaminski et al. [21] and because deviations from this range yielded spurious numerical errors in the shear wave splitting calculations described below.

3.2. Predicted shear wave splitting

To provide predictions of SWS along raypaths in our models, we utilized the resulting elastic strain tensors acquired from the LPO development calculations to provide a map of flow-induced mantle fabric (e.g., [9,27,35,37]). Along each raypath, we solved the Christoffel equation along 10 km depth increments from source to receiver. We calculated predicted SWS by cross-correlating the predicted particle motions at the surface across a range of possible splitting times and fast polarization directions. The best-fitting splitting parameters are those that yield the most nearly singular covariance matrix, and thus the most nearly linear particle motion (e.g., [38]). To approximate the maximum depth of the dislocation creep/diffusion creep boundary below which LPO is predicted not to develop (e.g., [4]), we did not include splitting along raypath segments below 400 km depth.

4. Results of LPO and shear wave splitting modeling

Here we present our LPO development and predicted SWS results for flow models using anhydrous, hydrous, and anhydrous to hydrous transition slip systems. To examine anhydrous and hydrous mantle olivine LPO development, we used the critically resolved shear stresses from Kaminski and Ribe [5,6] for anhydrous olivine LPO development models and from Jung and Karato [4] for hydrous olivine models. We note that the simple flow fields used in our modeling are not viscosity-dependent; we, therefore, do not incorporate the effects of hydrated olivine in calculations of flow, but rather focus on the effects of hydration with regard to LPO development and predicted SWS.

4.1. Simple shear models

We first examined a simple shear model of Couette flow with prescribed velocity of unity at the upper boundary of the model, zero flow at the bottom, and a channel thickness of 50 km. We used a mineralogy composed of 70% olivine and 30% enstatite. To provide an improved intuition of the effects of LPO development on predicted SWS values, we particularly focus on the

evolution to stable shear wave splitting parameters in the models, or those parts of the model where LPO development and predicted splitting approach steady-state. We also note that using a range of M^* values between 50 and 200 slightly influences LPO development [21], but does not significantly modify predicted SWS results for any of the simple shear models discussed below. Finally, the reference frame in our model is

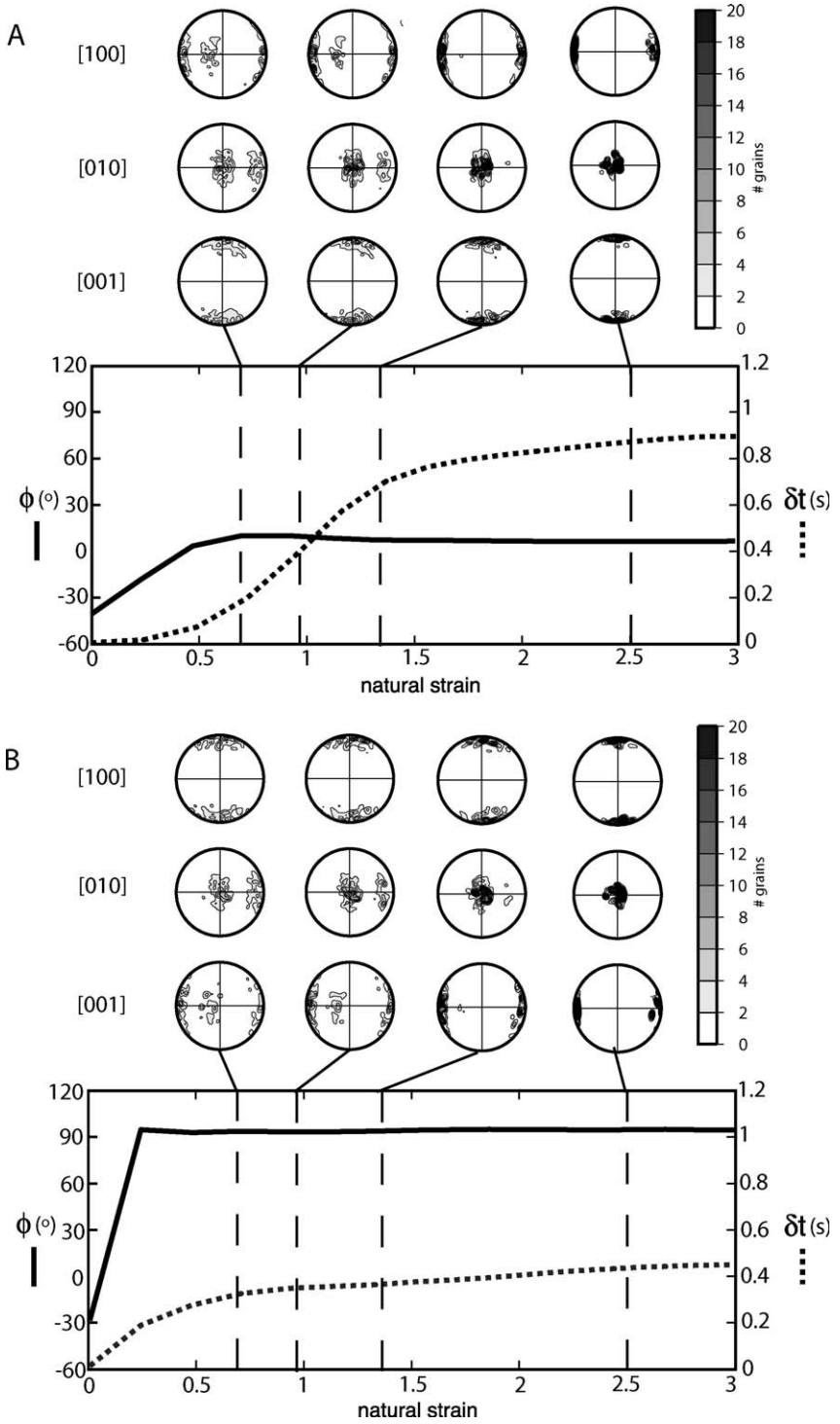

orthogonal to that used by Jung and Karato [4]; our pole figures for the [010] and [001] axes are therefore opposite to pole figures presented in their work.

4.1.1. Anhydrous olivine rheology

We first evaluated fabric development and predicted shear wave splitting for a model with the anhydrous olivine slip system (Fig. 2). In this model, LPO of the olivine/enstatite aggregate begins to stabilize at relatively low strains (Fig. 2A, upper panel). By a natural strain of 0.7 (~200% strain), significant populations of *a*-axes are aligned with an average orientation parallel to the shear direction. Conversely, LPO strength stabilizes at a larger natural strain of ~1.3 (~370% strain) as the bulk of *a*-axis orientations is more nearly parallel to the shear direction. Natural strains larger than 1.3 yield minimal increases in overall LPO strength.

Predicted SWS results for this model mirror the trends present in the LPO models (Fig. 2A, lower panel). Fast polarization directions are oriented parallel to the flow direction by a natural strain of ~0.5 (~165% strain). Splitting time values continue to increase to a natural strain of ~1.3 (~370% strain) and plateau at ~0.8 s. This result highlights the observation that the continued progression of fabric development influences splitting times despite the stability in fast polarization directions. However, beyond natural strains of ~1.3, splitting times do not increase significantly despite continued incremental development of LPO strength at larger strains.

4.1.2. Hydrous olivine rheology

In the hydrated olivine case, LPO development and predicted fast directions also stabilize at relatively low strains (Fig. 2B). As in the anhydrous model, LPO of the olivine/enstatite aggregate begins to stabilize at relatively low strains (Fig. 2B, upper panel). By a natural strain of 0.7 (~200% strain), significant populations of *a*-axes are aligned with an average orientation orthogonal to the shear direction. Conversely, LPO strength stabilizes at a larger natural strain of ~1.3 (~370% strain) as the bulk of *a*-axis orientations are more nearly orthogonal to the shear direction. Natural strains larger than 1.3 yield minimal increases in overall LPO strength.

Predicted SWS results for this model mirror the trends presented in the LPO models (Fig. 2B, lower panel). Fast polarization directions stabilize at relatively low strain values (natural strain of 0.25 or ~130% strain) and are oriented orthogonal to the shear direction, which are lower values relative to the anhydrous simple shear case above. Unlike the anhydrous olivine model, splitting time values maintain a slight but steady increase beginning at a natural strain of ~0.7 (~200% strain). At strains greater than ~200%, the splitting time continues to increase slightly to a value of 0.45 s, or ~25% smaller than that for the anhydrous case.

4.1.3. Transition from anhydrous to hydrous olivine rheology

In order to investigate the transition from anhydrous to hydrous olivine LPO development, we imposed a first-order change in olivine slip system following stability of LPO and shear wave splitting as determined by the anhydrous model (Fig. 3). At the transition, the shift from anhydrous (Fig. 3, points A and B) to hydrous olivine deformation appears as a rapid shift in LPO (Fig. 3, point C) as *a*-axis concentrations migrate from dominantly flow-parallel to sub-perpendicular to flow. Immediately following the transition, the LPO strength is reduced as the crystallographic axes begin to realign and *a*-axes are no longer parallel to the flow direction (Fig. 3, point D).

By a natural strain of ~0.4 (~150% strain) following the transition, reorientation of crystallographic axes is evident (Fig. 3, point D). As strain continues to increase, multiple populations of crystallographic axis concentrations develop during the continuing alignment orthogonal to flow (Fig. 3, points E and F). At a natural strain of 1.25 (~350% strain), *a*-axes are reoriented 90° to flow (Fig. 3, point G), while natural strains larger than 1.5 yield minimal increases in overall LPO strength (Fig. 3, point H).

Fig. 2. Lattice-preferred orientation (LPO) and predicted shear wave splitting for simple shear models with respect to strain. Shear direction is left–right in the plane of the page. (Upper half of each figure) Lower hemisphere pole projections for olivine aggregates showing the progression of LPO. Darker colors represent larger populations of crystallographic axis concentrations for [100], [010], and [001] axes. (Lower half of each figure) Predicted shear wave splitting parameters showing effects of LPO changes. Solid line denotes fast polarization direction values; dashed line denotes splitting time values. We note that the reference frame in the model is orthogonal to that in Jung and Karato [4], so axes [010] and [001] appear orthogonal to those in Jung and Karato [4]. (A) Anhydrous model. Pole figures demonstrate *a*-axes aligning in the direction of shear and of increasing LPO development with strain. Fast polarization directions stabilize rapidly at a natural strain value of ~0.7 (~200% strain), while splitting times reflect the continued progression of LPO and stabilize at a natural strain value of ~1.3 (~370% strain). (B) Hydrous model. Pole figures show *a*-axes aligning orthogonally to the direction of shear and of increasing LPO development with strain. Fast polarization directions stabilize more slowly than the anhydrous model at a natural strain value of ~0.25 (~130% strain), while splitting times reflect the continued progression of LPO and stabilize at a natural strain value of ~0.7 (~200% strain).

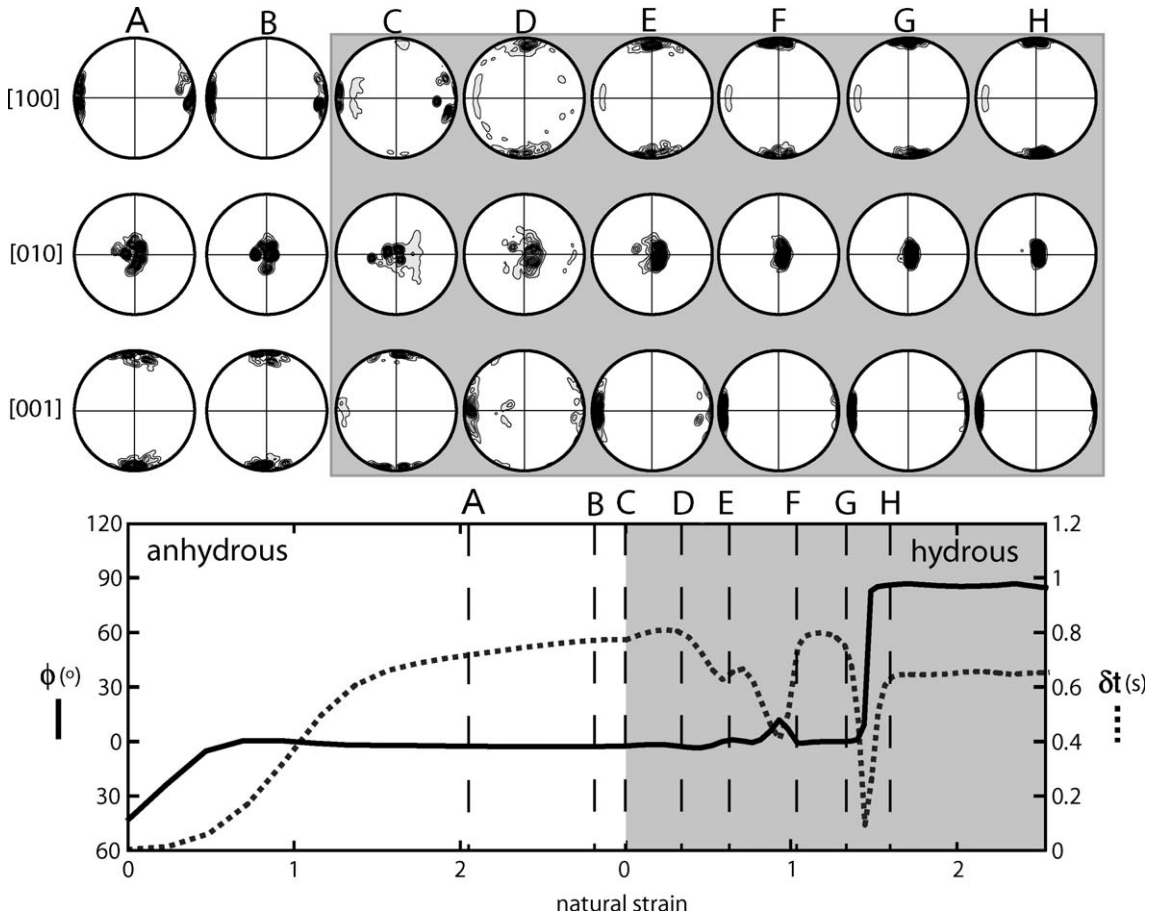

Fig. 3. Lattice-preferred orientation (LPO) and predicted shear wave splitting with respect to strain for anhydrous to hydrous transition in simple shear models. See Fig. 2 for plot details. Transition from anhydrous to hydrous mineralogy occurs at point C. Following the transition, LPO restabilizes rapidly at small strains, while predicted shear wave splitting parameters restabilize rapidly but at a larger strain value of ~1.25–1.5 (~350–450% strain) (between points G and H).

Predicted SWS results clearly reflect the shift in olivine slip systems. Fast polarization directions for regions near the transition shift from flow parallel to flow orthogonal orientation by a natural strain of ~1.3 (~370% strain) (Fig. 3, points G and H). After shear wave splitting parameters restabilize in the hydrous olivine regime, splitting times are ~0.2 s (~50%) greater than the final value in the hydrous olivine case.

4.2. Subduction zone mantle wedge

To examine the development of LPO in a subduction zone mantle wedge, we utilize a simple, kinematic finite element flow model with isoviscous rheology as developed by Hall et al. [27] (Fig. 4). The model is 80 elements wide by 40 elements tall with a 45° dipping slab extending to a depth of 600 km. Zero normal stress boundary conditions are prescribed along the sides of the model, and a zero velocity boundary condition is prescribed along the bottom model boundary. The overriding plate is fixed, while the converging plate and subducting slab velocities are prescribed to a value of 10 cm/yr. No back-arc spreading is assumed in these models.

The resulting flow field primarily consists of two major convection cells (Fig. 4). One cell develops between the subducting slab and the overriding plate with the mantle wedge, while a second cell develops behind the slab and beneath the converging plate. In this study, we focus on the mantle wedge convection cell and examine the evolution of LPO development and predicted shear wave splitting from this flow model assuming a mineralogy comprised of 70% olivine and 30% enstatite. Similar to the simple shear study, we investigated anhydrous and hydrous olivine

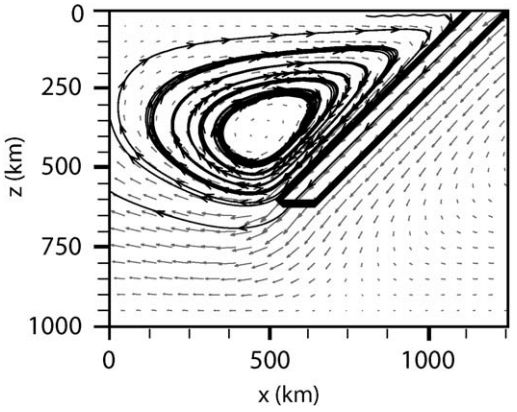

Fig. 4. Velocity field for finite element subduction zone flow model described in text and in Hall et al. [27]. Thin vectors represent velocity values within model; thick lines represent individual particle paths through the velocity field.

rheologies as well as a range of anhydrous–hydrous transitions within the mantle wedge. We utilized the field of elastic strain tensors determined by DRex in a grid within the mantle wedge. For models with anhydrous and hydrous olivine rheologies, we determined SWS predictions for shear phases using synthetic raypaths at receivers every 100 km from the trench and events at 100 km increments from the trench along the surface of the subducting slab (Fig. 5A).

4.2.1. Anhydrous mantle wedge

We first evaluated fabric development and predicted shear wave splitting for the case of a subduction zone mantle wedge with the anhydrous olivine slip system (Fig. 5B and D). Along many parts of the mantle wedge, particularly the upper plate and slab–wedge interfaces, *a*-axes are aligned approximately parallel to the flow direction (Fig. 5B and C). LPO is not as well organized in regions of high strain and/or large velocity gradients, such as in the center of and the extreme corner of the wedge.

Predicted SWS parameters for this model exhibit fast polarization directions parallel to the flow direction and splitting times that show a simple increase with path length (Fig. 5C). Splitting times for the station 100 km from the trench are small values that are effectively null measurements. Generally, null measurements occur as a result of weak or no anisotropy, complex anisotropy, or incoming shear wave polarization parallel or perpendicular to the fast direction. In this model, null measurements likely result from complex anisotropy and incoming polarization direction.

4.2.2. Hydrous mantle wedge

We next examined fabric development and predicted shear wave splitting for the case of a subduction zone mantle wedge with a hydrous olivine slip system (Fig. 6). Along many parts of the mantle wedge, particularly the upper plate and slab-wedge interfaces, *a*-axes are aligned orthogonal to the flow direction (Fig. 6B and C). LPO is not as well organized in regions of high strain and/or large velocity gradients, such as in the center of and the extreme corner of the wedge. Along the slab, the *a*-axes are aligned approximately trench-parallel and do not exhibit the slab-parallel dip seen in the anhydrous case (Fig. 6A). Areas of high strain and sharp velocity gradients are also reflected in *a*-axes orientations where LPO concentrations become less well organized (Fig. 6A and B). The maintenance of flow-orthogonal *a*-axes is not surprising, since the soft-deformation axis is aligned parallel to flow and accommodates much of the strain (Fig. 6A and B). Predicted SWS parameters for this model at all stations exhibit fast polarization directions orthogonal to the flow direction. Splitting times exhibit a simple increase with path length (Fig. 6C) and are well resolved throughout the model.

4.2.3. Transitions from anhydrous to hydrous mantle wedge

We evaluated LPO development models with anhydrous to hydrous transitions in the mantle wedge to represent the broad range of distances between trenches and volcanic fronts found in subduction settings (e.g., [39,40]). We focus on transitions at 100 km, 150 km, and 250 km from the trench that extend to the surface of the subducting slab. While mantle wedges are likely not fully hydrated as assumed in these models, we examine these end-member models as estimates of the maximum effects of LPO development in hydrated systems. For these models, we predicted shear wave splitting values within the wedge using both station and event spacing of 25 km each to capture potential SWS variations due to the transitions (Fig. 7A).

4.2.3.1. 100 km hydrous mantle wedge. We first examine the effects of LPO development with a mantle wedge possessing the hydrous olivine slip system 100 km beyond the trench (Fig. 7). Near the overriding plate, LPO development and predicted *a*-axis flow-parallel orientation in the anhydrous portion of the mantle wedge are nearly identical to those observed in the anhydrous wedge (Fig. 7B). At the transition, *a*-axes in the upper 50 km of the mantle wedge are not aligned

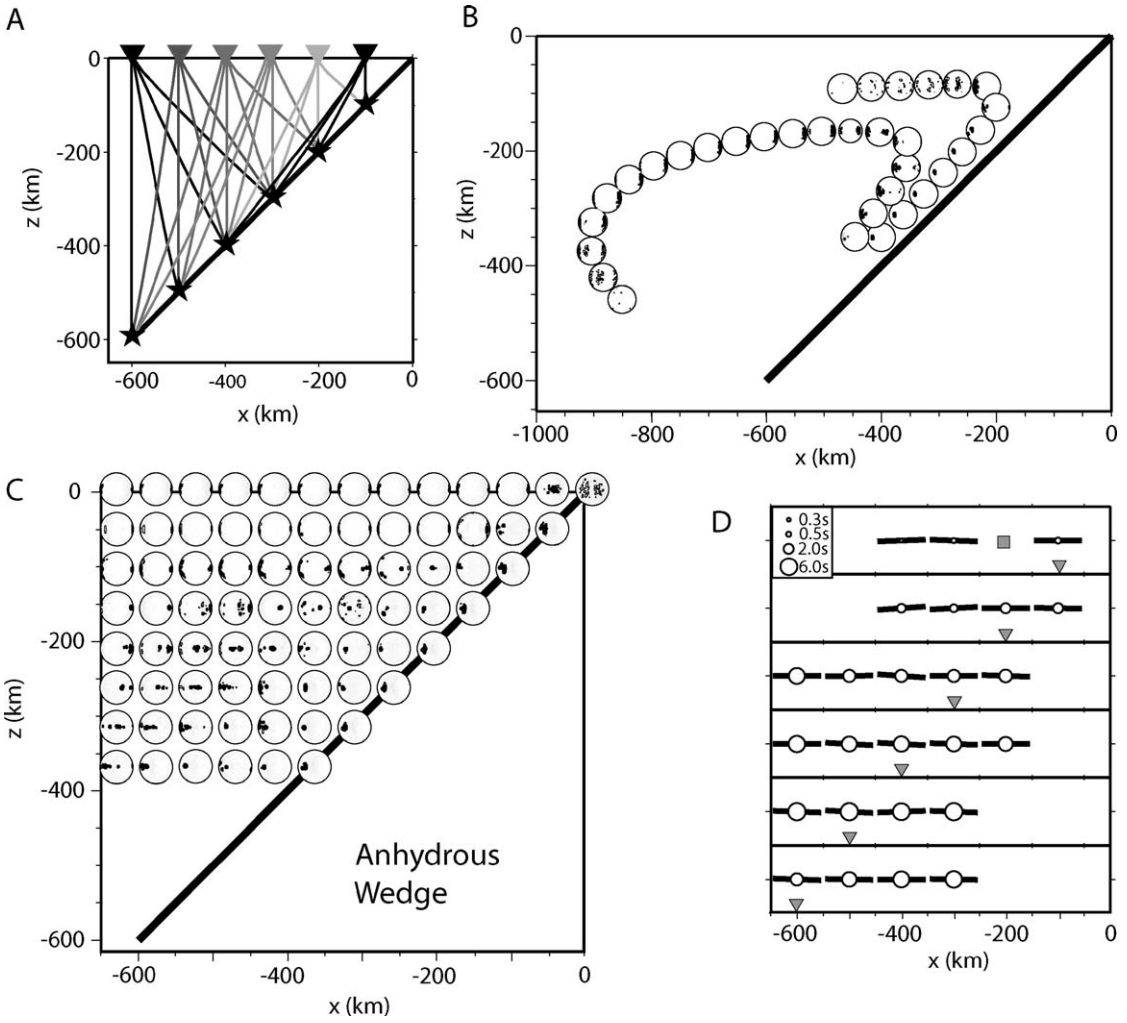

Fig. 5. LPO development and shear wave splitting results for the anhydrous subduction zone flow model. (A) Raypaths used for shear wave splitting predictions. Receivers (inverted triangles) and events (stars) are spaced at 100 km increments. Grayscale path shades coordinate with receiver. (B) Examples of the evolution of *a*-axis LPO along individual particle paths within the model. Each streamline represents a total maximum natural strain value of 5. These examples show smooth evolution of LPO along a path including flow around the mantle wedge corner. (C) Map view of lower hemisphere project of pole figures of *a*-axis LPO for olivine/enstatite aggregates in the model delimited to every 6 points within the model grid. Pole figures are not shown below 400 km depth based on the assumption that dislocation creep does not occur below this depth. *a*-axes align with the flow direction with the exception of parts of the center of the convection cell as well as near regions of strong velocity gradients such as in the mantle wedge corner. (D) Predicted shear wave splitting results for raypaths in panel (A). Azimuths of bars represent the orientation of the fast polarization direction; white circles are scaled to splitting time. Value on left of figure represents station location relative to trench; splitting parameters are plotted at event epicenters. Fast polarization directions are flow-parallel for all raypaths. Splitting times exhibit a first-order path length dependence, with longer paths corresponding to larger splitting times. Very small splitting values exist for paths sampling near the corner of the model where LPO is changing rapidly.

to the flow direction. In the lower 50 km of the wedge at the transition, *a*-axes are aligned orthogonal to flow (Fig. 7B). The orientation of *a*-axes within the hydrated wedge is orthogonal to flow. Away from the hydrated portion of the wedge, *a*-axes remain oriented orthogonal to flow (Fig. 7B). Within 50 km away from the transition on the anhydrous wedge side, *a*-axes begin to reorient parallel to flow (Fig. 7B).

Predicted SWS results for this model clearly reflect the anhydrous–hydrous transition (Fig. 7C). Effects of the transition are evident out to the receiver 200 km from the trench, or approximately 100 km from the transition. Stations located 25–100 km from the trench exhibit flow-orthogonal fast directions only and splitting times that generally increase with path length, ranging from 0.25 to

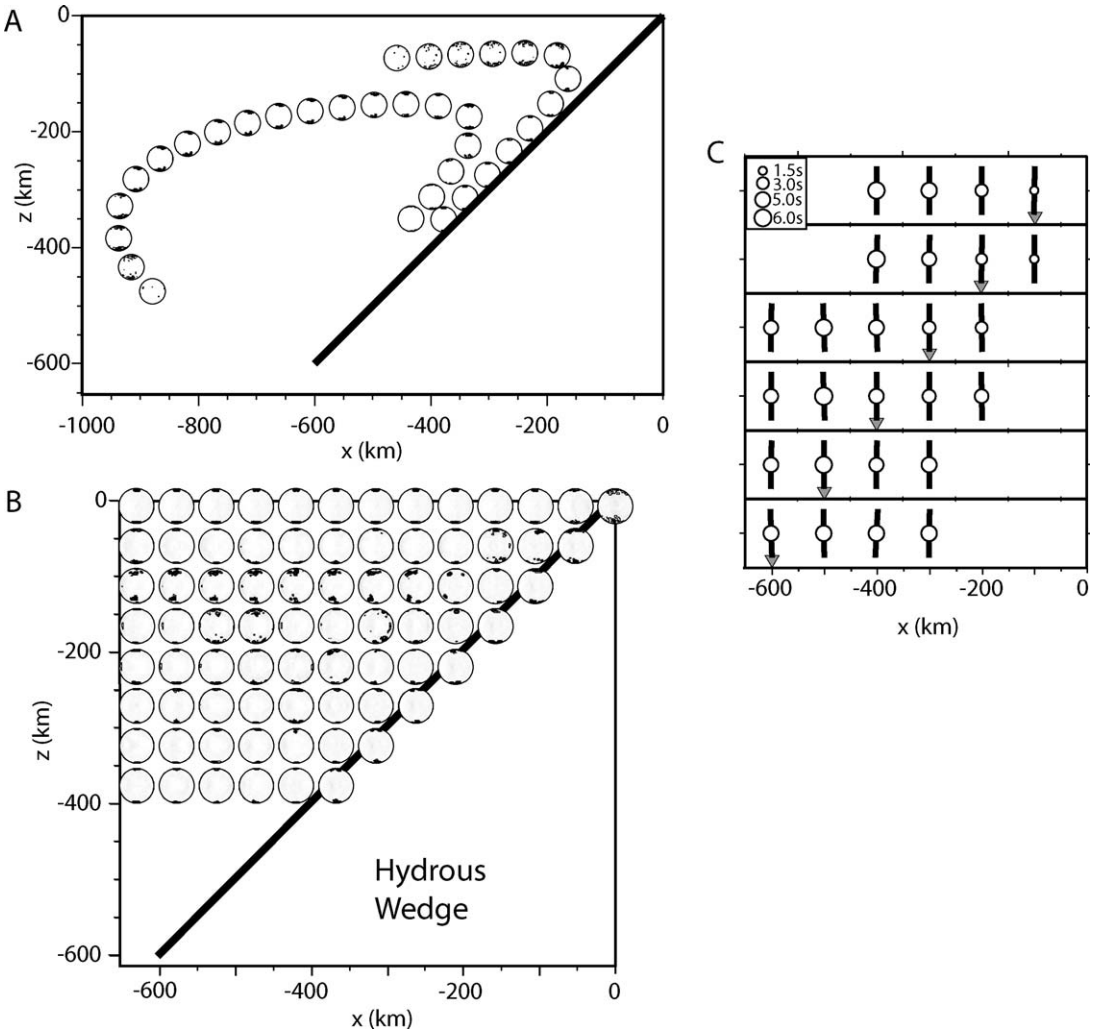

Fig. 6. LPO development and shear wave splitting results for the hydrous subduction zone flow model. (A) Examples of the evolution of *a*-axis LPO along individual particle paths within the model. Each streamline represents a total maximum natural strain value of 5. These examples show smooth evolution of LPO along a path including flow around the mantle wedge corner. (B) Pole figures of *a*-axis LPO for olivine/enstatite aggregates in the model delimited to every 6 points within the model grid. Pole figures are not plotted below 400 km depth based on the assumption that dislocation creep does not occur below this depth. *a*-axes align with the flow direction with the exception of parts of the center of the convection cell as well as near regions of very strong velocity gradients such as in the mantle wedge corner. (C) Predicted shear wave splitting results for raypaths in Fig. 5A. Azimuths of bars represent the orientation of the fast polarization direction; white circles denote splitting time. Value on left of figure represents station location relative to trench; splitting parameters are plotted at event epicenters. Fast polarization directions are flow-orthogonal (trench-parallel) for all raypaths. Splitting times exhibit a first-order path length dependence with longer paths corresponding to larger splitting times.

1.35 s. Stations 125–200 km from the trench exhibit roughly trench-parallel fast directions near the transition, but rotate to flow-parallel within 25–50 km from the transition in the anhydrous portion of the wedge. These results also correspond with the evolution of *a*-axis orientations in this portion of the model (Fig 7B). Splitting times for this subset of stations reflecting the transition are relatively weak, and include both null measurements as well as resolvable splitting times ranging from 0.25 to 1.0 s. Stations 225 km from the trench and beyond exhibit flow-parallel fast directions only, and differences in splitting times that are larger for those raypaths most nearly orthogonal to the *a*-axis direction in the model.

4.2.3.2. 150 km hydrous mantle wedge. We next examine the effects of LPO development with a mantle wedge possessing the hydrous olivine slip system 150 km beyond the trench (Fig. 8). LPO development

and predicted *a*-axis flow-parallel orientation in the anhydrous portion of the mantle wedge near the overriding plate are nearly identical to those observed in the anhydrous wedge (Fig. 8A). At the transition, *a*-axes for locations directly beneath the overriding plate are orthogonal to flow. The *a*-axes within the hydrated wedge as well as in the lower 75 km of the transition are orthogonal to flow (Fig. 8A). Away from the hydrated wedge, *a*-axes remain oriented orthogonal to flow (Fig. 8A). There is no clear re-alignment of axes

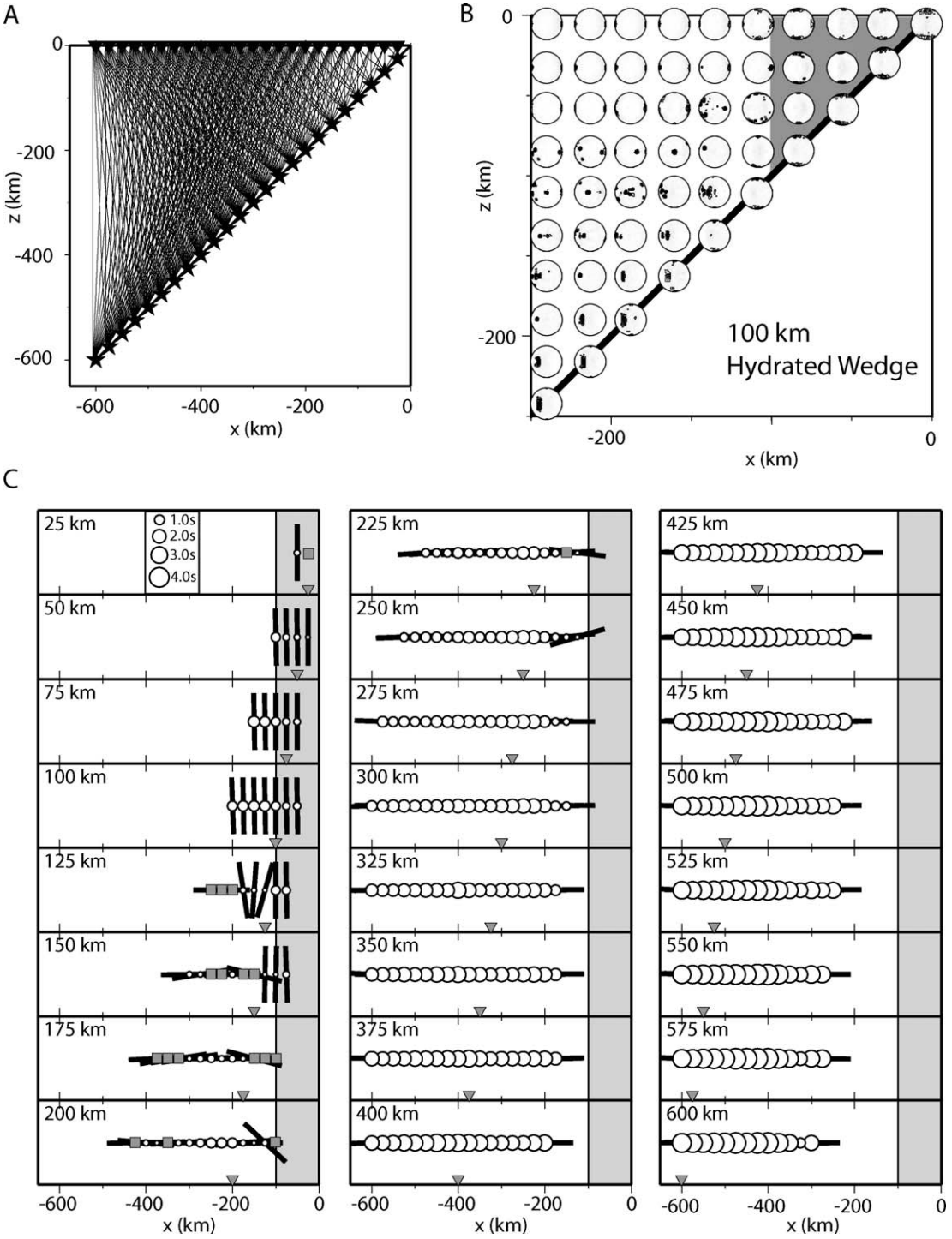

away from the transition; however, many of the axes are nearly flow-parallel within 75–100 km of the transition (Fig. 8A).

Predicted SWS results for this model also clearly reflect the anhydrous–hydrous transition (Fig. 8B). Effects of the transition are evident out to the receiver 250 km from the trench, or approximately 150 km from the transition. Stations located 25–150 km from the trench exhibit flow-orthogonal fast directions and splitting times that generally increase with path length, ranging from 0.7 to 1.4 s. The station 175 km from the trench shows a decrease in splitting time from 1.35 to 0.75 s, while fast directions are flow orthogonal. Stations 200–225 km from the trench exhibit trench-parallel fast directions near the transition, but rotate to a flow-parallel orientation within 25–50 km of sampling the anhydrous wedge. These stations best show the transition from flow-parallel to trench-parallel fast directions. Splitting times for this subset of stations reflecting the transition are relatively weak, and includes resolvable splitting times ranging from 0.3 to 1.15 s. Stations 250 km from the trench and beyond exhibit flow-parallel fast directions only, and differences in splitting times which are larger for those raypaths most nearly orthogonal to the *a*-axis direction in the model.

4.2.3.3. 250 km hydrous mantle wedge. We finally examine the effects of LPO development with a mantle wedge possessing the hydrous olivine slip system 250 km beyond the trench (Fig. 9). LPO development and predicted *a*-axis flow-parallel orientation in the anhydrous portion of the mantle wedge near the overriding plate (Fig. 9A) are nearly identical to those observed in the anhydrous wedge. At the transition, *a*-axes for locations directly beneath the overriding plate are orthogonal to flow. The *a*-axes within the hydrated wedge as well as in the lower 75 km of the transition are orthogonal to flow (Fig. 9A). Upon exiting the hydrated wedge, *a*-axes remain oriented orthogonal to flow (Fig. 9A). There is no clear re-alignment of axes away from the transition; however, many of the axes are nearly flow-parallel within −75 to 100 km (Fig. 9A).

Predicted SWS results for this model also clearly reflect the anhydrous–hydrous transition (Fig. 9B). Effects of the transition are evident out to the receiver 425 km from the trench, or approximately 175 km from the transition. Stations located between 25 and 250 km from the trench exhibit flow-orthogonal fast directions and splitting times that generally increase with path length, ranging from 0.7 to 1.4 s. The station at 275 km from the trench shows a decrease in splitting time, from 1.35 to 0.75 s, while fast directions are flow orthogonal. Stations 325–375 km from the trench exhibit trench-parallel fast directions near the transition, but rotate to a flow-parallel orientation within 25–125 km of sampling the anhydrous wedge. These stations best show the transition from flow-parallel to trench-parallel fast directions. Splitting times for this subset of stations reflecting the transition are relatively weak, and includes resolvable splitting times ranging from 0.3 to 1.15 s. Stations 450 km from the trench and beyond exhibit flow-parallel fast directions only, and differences in splitting times which are larger for those raypaths most nearly orthogonal to the *a*-axis direction in the model.

5. Shear wave splitting and mantle fabric in hydrated subduction systems

The results of our LPO modeling and SWS predictions place important constraints on our understanding of the links between flow dynamics and seismic observations used to infer flow. While the underlying models in this work are relatively simple and certainly do not fully represent all details of Earth dynamics, they provide an important set of guidelines in understanding LPO development and its relationship with SWS, particularly in subduction zone environments where hydrated mantle phases likely play important roles.

5.1. Shear wave splitting in hydrous–anhydrous transitions

Our simple shear experiments for transitions from anhydrous to hydrous olivine suggest that moderate

Fig. 7. LPO development and shear wave splitting results for the 100 km wide anhydrous–hydrous transition subduction zone flow model. (A) Raypaths used for shear wave splitting predictions. Receivers (inverted triangles) and events (stars) are spaced at 25 km increments. (B) Pole figures of *a*-axis LPO for olivine aggregates in the model delimited to every 6 points within the model grid. Pole figures are not plotted below 400 km depth based on the assumption that dislocation creep does not occur below this depth. *a*-axes align with the flow direction with the exception of parts of the center of the convection cell as well as near regions of very strong velocity gradients and a change in olivine slip system in the mantle wedge corner. (C) Predicted shear wave splitting results for raypaths in panel (A). Solid line represents location of anhydrous–hydrous transition. Azimuths of bars represent the orientation of the fast polarization direction; white circles denote splitting time. Value on left of figure represents station location relative to trench, as does the location of the inverted triangle; splitting parameters are plotted at surface projection of hypocenter. Fast polarization directions and splitting times change significantly with sampling region and highlight the existence of the transition. See Section 4.2.3.1 for further details.

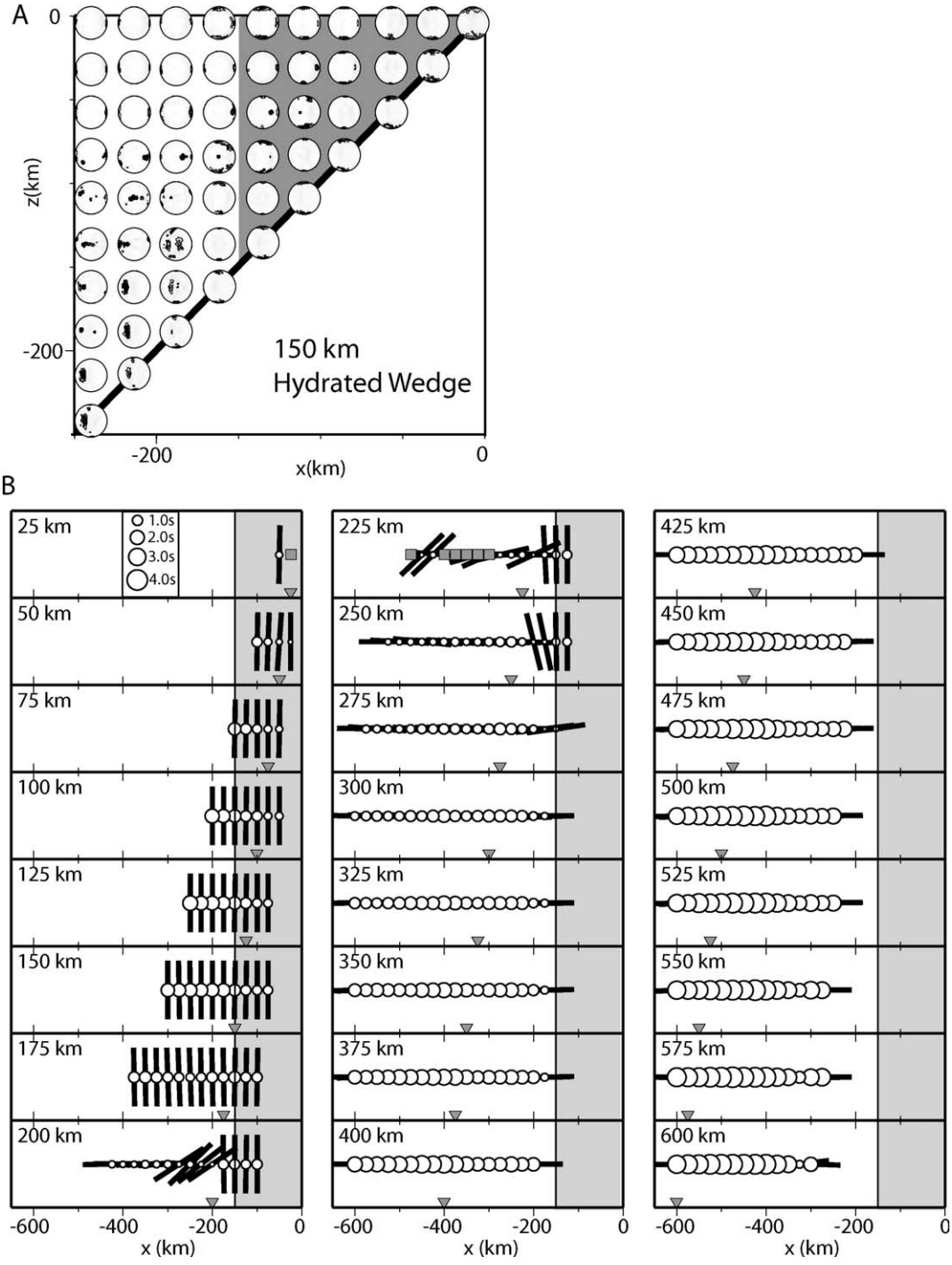

Fig. 8. LPO development and shear wave splitting results for the 150 km wide anhydrous–hydrous transition subduction zone flow model. For (A) and (B), please see description in Fig. 7B and C and see Section 4.2.3.2 for further details.

strains are required to provide significant manifestation of the transition. LPO evolves to steady state after ~145% strain (Fig. 3, points C and D), while predicted significant changes in fast directions are evident after ~370% strain. In order to achieve resolvable flow-orthogonal fast directions, a ~370–~450%

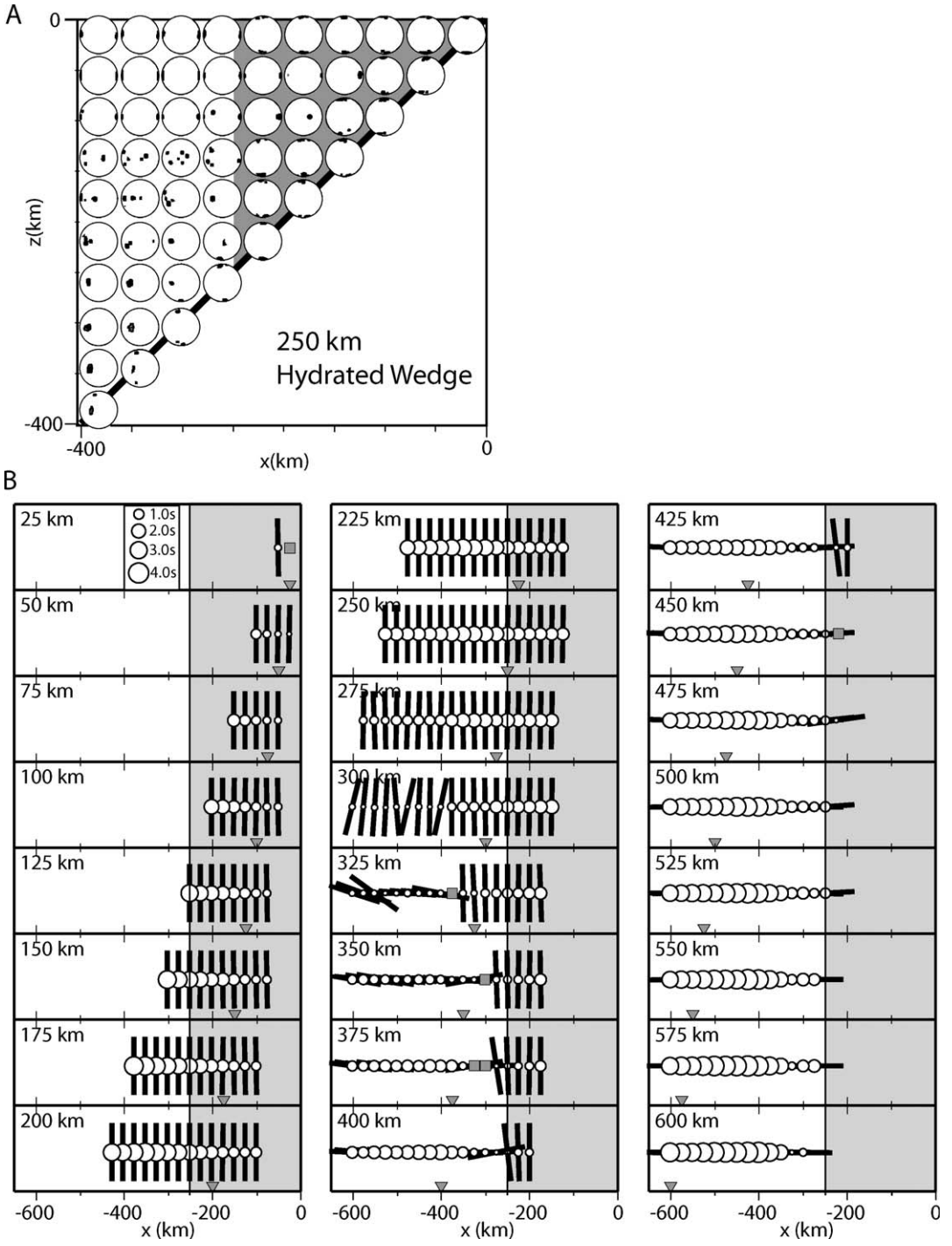

Fig. 9. LPO development and shear wave splitting results for the 250 km wide anhydrous–hydrous transition subduction zone flow model. For (A) and (B), please see description in Fig. 7B and C and see Section 4.2.3.3 for further details.

increase in strain is required. Conversely, patterns of splitting time and null measurement variations reveal the transition after only ~150% strain (Fig. 3, point D).

Using these results as a guide for regions of subduction systems that may contain a transition from anhydrous to hydrated mantle, we utilize a combination of fast direction and splitting time variations to identify

the location of the transition. For these models, fast directions orient orthogonally to the convergence direction within 50 km of the transition (Fig. 7C) for the smaller 100 km hydrous wedge. Fast directions orient orthogonally within 50 km (Fig. 8B) to 75 km (Fig. 9B) for the larger hydrous wedges.

Trends in splitting time are more complex, and vary significantly between models. For all models, splitting times for stations above the hydrous portion of the wedge increase away from the trench. Depending upon the horizontal extent of the hydrated wedge splitting time trends vary for stations above the transition and away from the hydrated wedge. In the 100 km wide hydrous wedge case (Fig. 7), stations 25–75 km away from the transition exhibit very small splitting times and many null measurements. In the 150 km wide hydrous wedge case (Fig. 8), very small splitting times and nulls are predicted for stations 50–100 km from the transition. For the 250 km wide hydrous wedge case (Fig. 9), very small splitting times and nulls begin 50–125 km from the transition. These results demonstrate that the locations of transitions in fabric are less easily identified for models with wider hydrated wedge models. We note that it is important to utilize both fast direction and splitting time variations to locate the vicinity of the anhydrous–hydrous transition. In these simple models, the use of both splitting parameters can improve the identification of the transition by up to 25–50 km.

5.2. Shear wave splitting in subduction systems

The results of these analyses highlight the importance of dense sampling of mantle wedge structure to adequately identify the location of potential anhydrous–hydrous transitions. Recognizing that this level of sampling density is not currently available for most subduction systems, we examine regions where the transition may be invoked as a viable mechanism for interpreting shear wave splitting variations. Many studies of subduction regions are consistent with our models (e.g., [41]) but conclusive comparisons are not possible since the wedge is primarily sampled by SKS phases in many studies. Therefore, we focus on three subduction regions, including Tonga, Japan, and Kamchatka, where mantle wedge hydration is likely a dominant process and the density of shear wave splitting observations is significant.

In the Tonga subduction zone, SWS results range from trench parallel near the trench to convergence parallel closer to the back-arc (Fig. 1, region A) (e.g., [8,10,42]). The presence of complex mantle wedge flow from a slab tear to the north of the region and southward-directed mantle flow, possibly from the Samoan plume, has been suggested as the cause of the observed variations [10]. Alternatively, Jung and Karato [4] suggested that hydration of olivine aggregates may influence the mantle fabric pattern close to the trench. The results of our anhydrous–hydrous transition modeling exhibit a predicted fast polarization direction pattern similar to the observed range for Tonga. However, our models do not predict the rapid increase in splitting times for raypaths that sample near the trench (Figs. 7–9). Mantle wedge hydration near the trench could, therefore, influence regional mantle fabric, but the large observed splitting times are more difficult to reconcile with our simple models.

SWS observations in Japan also range from trench-parallel near the trench to convergence-parallel in the back-arc (Fig. 1, region D) (e.g., [11,12,33,43–47]). This subduction system is more structurally complex than Tonga, however, as two triple junctions and multiple subducting slabs are present in the region. While crustal anisotropy may play a role in the local variability of splitting variations (e.g., [12,33,43]), mantle anisotropy is required to explain the bulk of the shear wave splitting results across the region (e.g., [12,33,44,48]). Near Hokkaido, Nakajima and Hasegawa [44] suggest that the splitting variations are a result of north–south shear in the overriding plate and/or the presence of a hydrated mantle wedge. Further south near Honshu and Ryukyu, Fouch and Fischer [33], Long and van der Hilst [48], and Bernot and Fouch [12] observe similar SWS trends of fast directions that rotate from trench-parallel near the trench to trench-orthogonal into the back-arc. Fouch and Fischer [33] obtained local S and teleseismic SKS splitting results and suggested that trench-parallel fast directions near Honshu may be the result of complex flow along the subduction interface. Results from a higher-density data set for Honshu by Bernot and Fouch [12] suggest that trench-parallel fast directions from local S phases may be caused by hydrated mantle fabric. Similarly, Long and van der Hilst [48] interpret a similar origin for trench-parallel fast directions using SKS phases; however, these phases also sample the subslab mantle which limits the depth resolution of seismic anisotropy in their study. SWS patterns for this region are consistent with our predictions from our transition cases (Figs. 7–9). Overall, splitting time data yields no clear trends for most studies, making comparison of splitting time observations with our predicted splitting time trends for the presence of a hydrated wedge is difficult. However, the variation in

fast polarization directions across the regions makes Japan a region where mantle hydration likely plays an important role in shear wave splitting variations.

SWS results in Kamchatka (Fig. 1, region E) exhibit small-scale variations in fast directions ranging from convergence-parallel near the trench to trench-parallel toward the back-arc. These splitting observations also contain a large number of relatively small splitting times and large numbers of null measurements [13,14]. Levin et al. [14] interpreted these results as due to a complex flow regime with mantle flow moving around the northern bending edge of the downgoing slab due to slab loss/detachment, possibly combined with deformation of material in the wedge containing small-scale melt pockets that generate the observed seismic anisotropy. Our model results, however, suggest that hydration may be a feasible explanation for measurements further from the trench, based on the small splitting time values and fast directions that rotate toward trench-parallel away from the trench (Figs. 8c and 9c). We suggest that further testing of these models may demonstrate that LPO in hydrous mantle phases may help explain the variation in shear wave splitting observations in this region. In order to fully evaluate possible hydration effects in the back-arc region, further constraints on seismic anisotropy are necessary for regions away from the trench and beyond the back-arc.

The results of our modeling present hydration as a possible mechanism to explain subduction zone shear wave splitting observations. Effects of hydration may not account for all variations in observed SWS (e.g., [45]), but this work provides a viable mechanism for altering deformation conditions in the mantle wedge. We, therefore, submit that hydration is a feasible mechanism for altering seismic anisotropy of the mantle wedge, but more detailed seismic data sets and further modeling efforts are necessary in order to further test this hypothesis as discussed in the next section.

5.3. Future directions

The models presented here represent new progress in modeling complex systems of LPO development and predictions of shear wave splitting. The models presented here are an important step in the development of more complex scenarios and will enable interpretation of these models in terms of both LPO development and shear wave splitting. However, many avenues could be pursued to provide more comprehensive models of the effects of water on flow, LPO development, and seismic anisotropy. Firstly, the presence of water in the mantle causes a reduction in mantle viscosity (e.g., [6,49]) and affects flow models (e.g., [25,50,51]). Incorporating a more realistic rheology in flow models that incorporates the hydrated portion of the mantle wedge, such as the recent work by Kneller et al. [52], and examining the feedback between these flow models and LPO development would be an important step. Examining the effects of partial melt, which may weaken LPO but strengthen SPO [53], should also be examined as a factor in both modifying the calculated flow field and the development of LPO. Secondly, the simple 2-D models shown here must be expanded. While 2.5-D flow models (e.g., [27]) enable somewhat more complex flow patterns, 3-D models with appropriate slab geometries and realistic rheologies would enable the examination of more complex flow regimes in a range of hydration settings. Finally, more robust predictions of shear wave splitting, such as full wave field methods (e.g., [54,55]) and surface wave methods (e.g., [56]) could significantly enhance predictions of seismic anisotropy in more complex models.

6. Conclusions

This study demonstrates that changes in LPO geometry due to transitions from anhydrous and hydrous olivine rheologies can be resolved with shear wave splitting provided appropriate sampling coverage of the mantle wedge. In simple shear models, complete reorientation of olivine aggregates due to a transition between anhydrous and hydrous olivine rheologies requires strains on the order of 370–450%. Continued LPO development can be observed in these models via increases in predicted splitting times. In simple subduction zone models with anhydrous–hydrous transitions in the inner 100–250 km of the mantle wedge, changes in LPO geometry are clearly manifested through a combination of fast polarization direction and splitting time variations specific to the model geometry. While other models can explain some of the significant variations in shear wave splitting in subduction zones, a transition between anhydrous and hydrous olivine rheologies provides a viable mechanism for these observed variations in some cases.

Acknowledgements

We express our gratitude to Karen Fischer for the predicted shear wave splitting code and David Abt and Karen Fischer for an early version of the shear wave splitting compilation presented in Fig. 1. Thanks also to

Megan Anderson, Lara Wagner, George Zandt and Susan Beck for fruitful discussions. We also thank Jules Browaeys for help with the LPO plotting and Mark Stevens for computer support. Martha Savage and an anonymous reviewer provided helpful comments that strengthened the clarity and conclusions of this work. MARGINS. Subduction Factory meetings in Eugene, Oregon and Honolulu, Hawaii inspired this work, and National Science Foundation grant EAR-0305564 provided funds for this research. We also express our gratitude to Simon Peacock for helpful discussions and support via National Science Foundation grant EAR-0215565.

References

[1] M. Bystricky, K. Kunze, L. Burlini, J.P. Burg, High shear strain of olivine aggregates: rheological and seismological consequences, Science 290 (2000) 1564–1567.
[2] M.K. Savage, Seismic anisotropy and mantle deformation; what have we learned from shear wave splitting? Rev. Geophys. 37 (1999) 65–106.
[3] A. Tommasi, Forward modeling of the development of seismic anisotropy in the upper mantle, Earth Planet. Sci. Lett. 160 (1998) 1–13.
[4] H. Jung, S. Karato, Water-induced fabric transitions in olivine, Science 293 (2001) 1460–1463.
[5] E. Kaminski, N.M. Ribe, A kinematic model for recrystallization and texture development in olivine polycrystals, Earth Planet. Sci. Lett. 189 (2001) 253–267.
[6] E. Kaminski, The influence of water on the development of lattice preferred orientation in olivine aggregates, Geophys. Res. Lett. 29 (2002) 1576.
[7] K.M. Fischer, M.J. Fouch, D.A. Wiens, M.S. Boettcher, Anisotropy and flow in Pacific subduction zone back-arcs, Pure Appl. Geophys. 151 (1998) 463–475.
[8] J.R. Bowman, M. Ando, Shear-wave splitting in the upper-mantle wedge above the Tonga subduction zone, Geophys. J. R. Astron. Soc. 88 (1987) 25–41.
[9] K.M. Fischer, E.M. Parmentier, A.R. Stine, E.R. Wolf, Modeling anisotropy and plate-driven flow in the Tonga subduction zone back arc, J. Geophys. Res. 105 (2000) 16181–116191.
[10] G.P. Smith, D.A. Wiens, K.M. Fischer, L.M. Dorman, S.C. Webb, J.A. Hildebrand, A complex pattern of mantle flow in the Lau backarc, Science 292 (2001) 713–716.
[11] Y. Hiramatsu, M. Ando, Seismic anisotropy near source region in subduction zone around Japan, Phys. Earth Planet. Inter. 95 (1996) 237–250.
[12] C.M. Bernot, M.J. Fouch, Seismic anisotropy and mantle flow beneath Japan, Fall Meet. Suppl. Abstract S52A-1056, Eos Trans. AGU 83 (2002).
[13] V. Peyton, V. Levin, J. Park, M.T. Brandon, J. Lees, E. Gordeev, A. Ozerov, Mantle flow at a slab edge: seismic anisotropy in the Kamchatka region, Geophys. Res. Lett. 28 (2001) 379–382.
[14] V. Levin, D. Droznin, J. Park, E. Gordeev, Detailed mapping of seismic anisotropy with local shear waves in southeastern Kamchatka, Geophys. J. Int. 158 (2004) 1009–1023.
[15] R.M. Russo, P.G. Silver, Trench-parallel flow beneath the Nazca plate from seismic anisotropy, Science 263 (1994) 1105–1111.
[16] J. Polet, P.G. Silver, S.L. Beck, T. Wallace, G. Zandt, S. Ruppert, R. Kind, A. Rudloff, Shear wave anisotropy beneath the Andes from the BANJO, SEDA, and PISCO experiments, J. Geophys. Res. 105 (2000) 6287–6304.
[17] M.L. Anderson, G. Zandt, E. Triep, M. Fouch, S. Beck, Anisotropy and mantle flow in the Chile–Argentina subduction zone from shear wave splitting analysis, Geophys. Res. Lett. 31 (2004) (art. no.-L23608).
[18] S. Karato, P. Wu, Rheology of the upper mantle: a synthesis, Science 260 (1993) 771–778.
[19] S. Zhang, S. Karato, Lattice preferred orientation of olivine aggregates deformed in simple shear, Nature 375 (1995) 774–777.
[20] R.D. Hyndman, S.M. Peacock, Serpentinization of the forearc mantle, Earth Planet. Sci. Lett. 212 (2003) 417–432.
[21] E. Kaminski, N.M. Ribe, J.T. Browaeys, D-Rex, a program for calculation of seismic anisotropy due to crystal lattice preferred orientation in the convective upper mantle, Geophys. J. Int. 158 (2004) 744–752.
[22] L. Mehl, B.R. Hacker, G. Hirth, P.B. Kelemen, Arc-parallel flow within the mantle wedge: evidence from the accreted Talkeetna arc, south central Alaska, J. Geophys. Res. 108 (2003).
[23] G.K. Batchelor, An Introduction to Fluid Dynamics, Cambridge University Press, Cambridge, UK, 1967, 615 pp.
[24] D. McKenzie, Finite deformation during fluid flow, Geophys. J. R. Astron. Soc. 58 (1979) 687–715.
[25] M.I. Billen, M. Gurnis, A low viscosity wedge in subduction zones, Earth Planet. Sci. Lett. 193 (2001) 227–236.
[26] M. Gurnis, C. Eloy, S.J. Zhong, Free-surface formulation of mantle convection: 2. Implication for subduction-zone observables, Geophys. J. Int. 127 (1996) 719–727.
[27] C.E. Hall, K.M. Fischer, E.M. Parmentier, D.K. Blackman, The influence of plate motions on three-dimensional back arc mantle flow and shear wave splitting, J. Geophys. Res. 105 (2000) 28009–28033.
[28] E.J. Garnero, T. Lay, D″ shear velocity heterogeneity, anisotropy and discontinuity structure beneath the Caribbean and Central America, Phys. Earth Planet. Inter. 140 (2003) 219–242.
[29] P.G. Silver, Seismic anisotropy beneath continents: probing the depths of geology, Annu. Rev. Earth Planet. Sci. 24 (1996) 385–432.
[30] M. Ando, Y. Ishikawa, F. Yamazaki, Shear wave polarization anisotropy in the upper mantle beneath Honshu, Japan, J. Geophys. Res. 88 (1983) 5850–5864.
[31] Y. Fukao, Evidence from core-reflected shear waves for anisotropy in the Earth's mantle, Nature (1984) 695–698.
[32] A. Fujimura, Preferred orientation of mantle minerals, in: S. Karato, M. Toriumi (Eds.), Rheology of Solids and of the Earth, Oxford Univ. Press, Oxford, 1989, pp. 263–283.
[33] M.J. Fouch, K.M. Fischer, Mantle anisotropy beneath northwest Pacific subduction zones, J. Geophys. Res. 101 (1996) 15987–916002.
[34] S. Karato, Seismic anisotropy due to lattice preferred orientation of minerals: kinematic or dynamic? in: M.H. Manghnani, S. Syono (Eds.), High-Pressure Research in Mineral Physics, Geophys. Monogr. Ser., vol. 39, AGU, Washington, DC, 1987, pp. 455–471.

[35] M.J. Fouch, K.M. Fischer, E.M. Parmentier, M.E. Wysession, T.J. Clarke, Shear wave splitting, continental keels, and patterns of mantle flow, J. Geophys. Res. 105 (2000) 6255–6275.
[36] H.-R. Wenk, K. Bennett, G.R. Canova, A. Molinari, Modeling plastic deformation of peridotite with the self-consistent theory, J. Geophys. Res. 96 (1991) 8337–8349.
[37] M.J. Fouch, K.M. Fischer, Shear wave anisotropy in the Mariana subduction zone, Geophys. Res. Lett. 25 (1998) 1221–1224.
[38] P.G. Silver, W.W. Chan, Shear wave splitting and subcontinental mantle deformation, J. Geophys. Res. 96 (1991) 16429–416454.
[39] R.J. Stern, Subduction zones, Rev. Geophys. 40 (2002) (art. no.-1012).
[40] R.D. Jarrard, Relations among subduction parameters, Rev. Geophys. 24 (1986) 217–284.
[41] E. Audoine, M.K. Savage, K. Gledhill, Anisotropic structure under a back arc spreading region, the Taupo Volcanic Zone, New Zealand, J. Geophys. Res. 109 (2004) (Art. No. B11305).
[42] K.M. Fischer, D.A. Wiens, The depth distribution of mantle anisotropy beneath the Tonga subduction zone, Earth Planet. Sci. Lett. 142 (1996) 253–260.
[43] Y. Hiramatsu, M. Ando, T. Tsukuda, T. Ooida, Three-dimensional image of the anisotropic bodies beneath central Honshu, Japan, Geophys. J. Int. 135 (1998) 801–816.
[44] J. Nakajima, A. Hasegawa, Shear-wave polarization anisotropy and subduction-induced flow in the mantle wedge of northeastern Japan, Earth Planet. Sci. Lett. 225 (2004) 365–377.
[45] D.K. Anglin, M.J. Fouch, Seismic anisotropy in the Izu–Bonin subduction system, Geophys. Res. Lett. 32 (2005).
[46] T. Iidaka, K. Obara, Shear-wave polarization anisotropy in the mantle wedge above the subducting Pacific plate, Tectonophysics 249 (1995) 53–68.
[47] E. Sandvol, J. Ni, Deep azimuthal seismic anisotropy in the southern Kurile and Japan subduction zones, J. Geophys. Res. 102 (1997) 9911–9922.
[48] M.D. Long, R.D. van der Hilst, Upper mantle anisotropy beneath Japan from shear wave splitting, Phys. Earth Planet. Inter. 151 (2005) 206–222.
[49] S. Karato, H. Jung, Water, partial melting and the origin of the seismic low velocity and high attenuation zone in the upper mantle, Earth Planet. Sci. Lett. 157 (1998) 193–207.
[50] J.A. Conder, D.A. Wiens, J. Morris, On the decompression melting structure at volcanic arcs and back-arc spreading centers, Geophys. Res. Lett. 29 (2002).
[51] C. Kincaid, I.S. Sacks, Thermal and dynamical evolution of the upper mantle in subduction zones, J. Geophys. Res. 102 (1997) 12295–12315.
[52] E.A. Kneller, P.E. van Keken, S. Karato, J. Park, B-type olivine fabric in the mantle wedge: insights from high-resolution non-Newtonian subduction zone models, Earth Planet. Sci. Lett. 237 (2005) 781–791.
[53] B.K. Holtzman, D.L. Kohlstedt, M.E. Zimmerman, F. Heidelbach, T. Hiraga, J. Hustoft, Melt segregation and strain partitioning: implications for seismic anisotropy and mantle flow, Science 301 (2003) 1227–1230.
[54] D. Abt, K.M. Fischer, Shear-wave splitting tomography in the Central American Mantle Wedge, Fall Meet. Suppl., Abstract T31D-05, Eos Trans. AGU, vol. 86, 2005.
[55] S.H. Hung, F.A. Dahlen, G. Nolet, Wavefront healing: a banana–doughnut perspective, Geophys. J. Int. 146 (2001) 289–312.
[56] D.A. Wiens, G.P. Smith, Seismological constraints on structure and flow patterns within the mantle wedge, in: J. Eiler (Ed.), The Subduction Factory, AGU Monograph, 2003, pp. 59–81.
[57] A. Brisbourne, G. Stuart, J.M. Kendall, Anisotropic structure of the Hikurangi subduction zone, New Zealand–integrated interpretation of surface-wave and body-wave observations, Geophys. J. Int. 137 (1999) 214–230.
[58] K. Gledhill, D. Gubbins, SKS splitting and the seismic anisotropy of the mantle beneath the Hikurangi subduction zone, New Zealand, Phys. Earth Planet. Inter. 95 (1996) 227–236.
[59] E.R. Klosko, F.T. Wu, H.J. Anderson, D. Eberhart-Phillips, T.V. McEvilly, E. Audoine, M.K. Savage, K.R. Gledhill, Upper mantle anisotropy in the New Zealand region, Geophys. Res. Lett. 26 (1999) 1497–1500.
[60] J. Xie, Shear-wave splitting near Guam, Phys. Earth Planet. Inter. 72 (1992) 211–219.
[61] X. Yang, K.M. Fischer, G.A. Abers, Seismic anisotropy beneath the Shumagin Islands segment of the Aleutian–Alaska subduction zone, J. Geophys. Res. 100 (1995) 18165–118177.
[62] S. Wiemer, G. Tytgat, M. Wyss, U. Duenkel, Evidence for shear-wave anisotropy in the mantle wedge beneath south central Alaska, Bull. Seismol. Soc. Am. 89 (1999) 1313–1322.
[63] J.F. Cassidy, M.G. Bostock, Shear-wave splitting above the subducting Juan de Fuca Plate, Geophys. Res. Lett. 23 (1996) 941–944.
[64] C.A. Currie, J.F. Cassidy, R.D. Hyndman, A regional study of shear wave splitting above the Cascadia subduction zone: margin-parallel crustal stress, Geophys. Res. Lett. 28 (2001) 659–662.
[65] C.A. Currie, J.F. Cassidy, R.D. Hyndman, M.G. Bostock, Shear wave anisotropy beneath the Cascadia subduction zone and western North American craton, Geophys. J. Int. 157 (2004) 341–353.
[66] R. Hartog, S.Y. Schwartz, Subduction-induced strain in the upper mantle east of the Mendocino triple junction, California, J. Geophys. Res. 105 (2000) 7909–7930.
[67] D.L. Schutt, E.D. Humphreys, Evidence for a deep asthenosphere beneath North America from western united states SKS splits, Geology 29 (2001) 291–294.
[68] R.M. Russo, P.G. Silver, M. Franke, W.B. Ambeh, D.E. James, Shear-wave splitting in Northeast Venezuela, Trinidad, and the eastern Caribbean, Phys. Earth Planet. Inter. 95 (1996) 251–275.